

Measurement of the inclusive hadroproduction cross section from proton-Al collisions at 12.9 GeV

Draft Version 0.1

27 Novembre 2004

Contents

1	Introduction	4
2	Physics Motivation	5
3	Harp forward spectrometer	7
3.1	Drift chambers	7
3.1.1	Alignment	7
3.1.2	Hit efficiency	7
3.2	Cherenkov	10
3.3	The TOF Wall	12
3.4	Electron identifier	13
4	Beam Detectors	15
5	Forward Tracking	16
5.1	The segment algorithm	16
5.2	The track reconstruction algorithm	17
5.3	Momentum measurement	20
5.4	Geometrical acceptance	21
5.5	Tracking efficiency	24
6	PID	28
7	Cross Section Calculation	28
8	Conclusions	28

Abstract

The HARP experiment at CERN has measured hadron yields in proton–nucleus collisions, for a variety of targets and beam energies. In this paper the inclusive cross section of light hadron (π, K) at proton beam energies of $12.9 \text{ GeV}/c$ and for a thin Al target of 5% interaction length is presented. The angular range considered are between 10 and 250 mrad , and between 0.5 and 10 GeV respectively. This result is relevant for the calculation of neutrino fluxes in the K2K experiment.

1 Introduction

The HARP experiment[1] was designed to perform a systematic and precise study of hadron production for beam momenta between 1.5 and 15 GeV/c and target nuclei ranging from hydrogen to lead. The detector was located at CERN, in the PS beam. The DAQ recorded 420 million events during the years 2001 and 2002.

The physics program of HARP includes: a) the measurement of pion yields for a variety of energies and targets relevant for the design of the proton driver of a future neutrino factory[2]; b) the measurement of pion yields on low Z targets as well as on cryogenic oxygen and helium targets, useful to improve the precision of atmospheric neutrino flux calculations[3]; and c) the measurement of pion and kaon yields, relevant for the calculation of the neutrino fluxes of experiments such as MiniBooNE[4] and K2K[5]. To this end a collaboration was set up with these groups. Beam energy settings and dedicated targets were used to provide the most relevant measurements.

HARP (Fig. 1) is a large acceptance spectrometer, with two distinct regions. In the forward part of the apparatus (up to polar angles of about 250 mrad), the main tracking devices are a set of large drift chambers. Magnetic analysis is provided by a 0.4 T dipole magnet and particle identification relies in the combination of a threshold Cherenkov detector, a time-of-flight wall and an electromagnetic calorimeter. In the rest of the solid angle the main tracking device is a TPC, which is complemented by a set of RPC detectors for time-of-flight measurements. The target is located inside the TPC. In addition, sophisticated beam instrumentation (including three timing detectors and threshold Cherenkov detectors) provides identification of the incoming particle and allows the interaction time at the target to be measured.

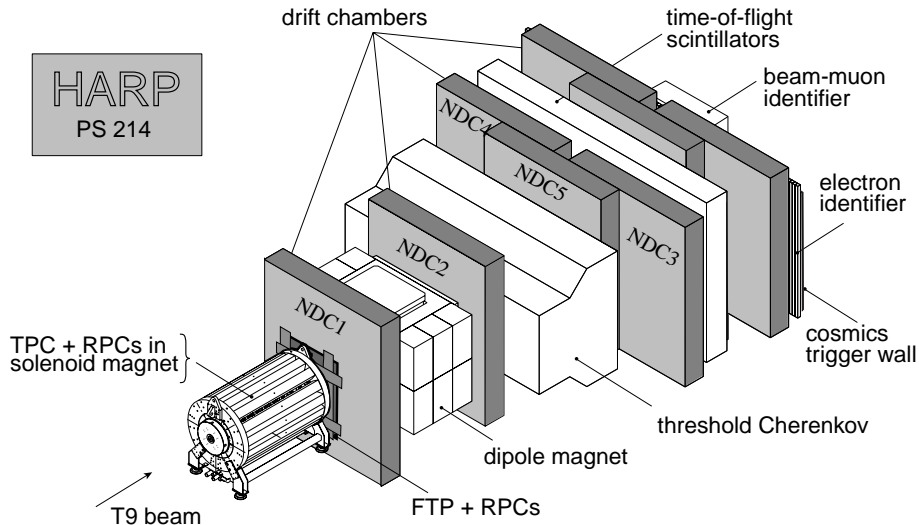


Figure 1: Schematic layout of the HARP spectrometer.

Given the immediate interest of the MiniBooNE and K2K experiments in a measurement of the production cross sections for pions and kaons at the energies and targets relevant for their beam setups, the HARP collaboration has given priority to the analysis of those particular data sets. In particular, we present in this article the measurement of the inclusive pion production cross section from proton-nucleus collisions, for a thin Al target ($5\% \lambda$) and a beam energy of 12.9 GeV . This measurement can be used as an ingredient of a calculation of the K2K neutrino flux

independent of their current technique[5]. Notice that the K2K neutrino beam is produced from the decay of hadrons (primarily pions) emanating from a 2λ Al target, at the KEK PS proton driver energies of 12.9 GeV. In addition to this measurement one would need a modelization or a measurement of the reinteractions in the long K2K target and a realistic description of the K2K neutrino beam line to provide an accurate prediction of the K2K flux. This will be the subject of forthcoming publications.

This paper is organized as follows. The physics motivation of the measurement is further discussed in section 2. Section 3 describes the various sub-systems making up the forward spectrometer, used for this analysis, while section 4 describes the beam detectors. The tracking algorithm in the forward region, central to this analysis is described in section 5, where we also compute the geometrical acceptance and tracking efficiency of the forward spectrometer. Particle identification is discussed in detail in 6. The ingredients making up the cross-section are discussed in 7. Our unfolding procedure is discussed in section ?? The calculation of the cross section itself is developed in ??. Conclusions are presented in section 8.

2 Physics Motivation

One of the main systematic errors on the neutrino oscillation parameters measured by the K2K experiment[5] comes from the uncertainty on the far/near neutrino flux ratio. This ratio depends on the differential pion production cross section, which, for pion energies above 2 GeV (corresponding to neutrino energy roughly above 1 GeV) is measured by a threshold Cherenkov detector with variable refraction index called pion monitor, or PIMON. For neutrino energies below 1 GeV, the far-near ratio is computed by means of a parameterization which fits very well the data in the region covered by PIMON. The systematic error comes from uncertainties in PIMON measurements as well as in the extrapolation to the low energy region, and can therefore be substantially improved by a precise measurement of the pion differential cross section covering all the relevant range of momentum and angle.

Fig. 2 (upper-left) shows a Monte Carlo simulation of the interacting neutrino spectrum at the K2K near detector assuming no oscillations. The experiment is very sensitive to variations of the predicted non-oscillated spectrum in the energy range between 0.5 and about 1 GeV/c , where the deformation of the spectrum due to the atmospheric oscillation is predicted to be maximal. Also shown in 2 is the pion production cross section corresponding to pions that result in neutrinos in the energy bin (0.5-0.75 GeV/c), where the oscillation is expected to peak (shaded bin in upper-left plot), according to the K2K Monte Carlo. Right-upper plot shows the momentum distribution, lower-left plot the angular distribution (in terms of the pion momentum and polar angle, e.g, the angle with respect to the proton axis) and bottom-right the correlated p - θ distribution. Notice that the relevant angular region is below 300 mrad, while the relevant momentum region is above 1 GeV. As it will be shown in section 7, this requirements are very well matched by HARP angular and momentum acceptance in the forward region. In consequence the HARP measurement can be immediately use to substantially reduce one of the leading errors in K2K.

3.5 million useful events were taken by HARP with incident 12.9 GeV/c protons and an exact replica of the K2K target, which is a 80×3 cm aluminum tube (2 interaction lengths). Another 6M events were collected with a $5\% \lambda$ aluminium target (“K2K thin target”) and a similar beam in order to decouple reinteraction and absorption effects from pure production. The analysis presented in this article is based on this particular setting.

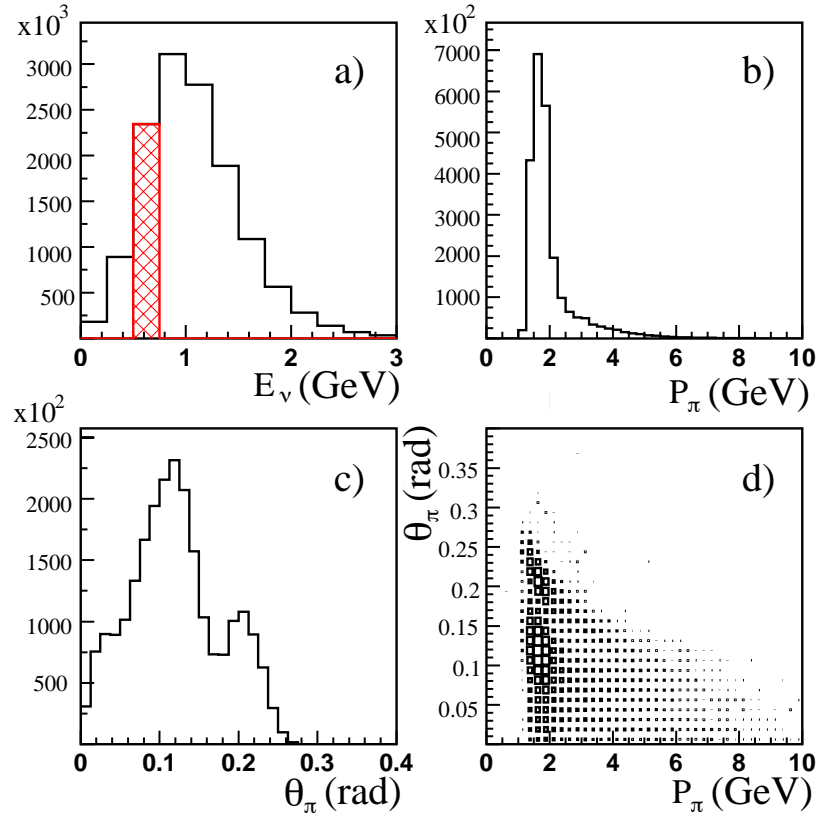


Figure 2: a) Neutrino spectrum at the K2K near detector. The peak of the oscillation correspond to the hatched bin. b) Momentum distribution of pions producing neutrinos with energies in the range 0.5-0.75 GeV/c. c) Angular distribution for the selected pions. d) Angle versus momentum for the selected pions. This plot, courtesy of the K2K collaboration

3 Harp forward spectrometer

In this section we briefly describe HARP forward detectors, concentrating on their performance for the current analysis. A more extensive description of the detectors, as well as the calibration procedures can be found in [6, 7, 8, 9, 10, 11].

3.1 Drift chambers

The main tracking device of the forward spectrometer is a set of drift chambers placed upstream and downstream of the dipole magnet. These chambers were recuperated from the NOMAD experiment, where they served both as a target for neutrino interactions and as a tracker for the produced charged particles. Their properties have been described elsewhere [12] and we will only describe here their hit performances in the HARP conditions (namely, with a less efficient but non-flammable gas mixture: Ar(90%)-CO₂(9%)-CH₄(1%), sense wires held at +1300V and potential wires at -2900V).

3.1.1 Alignment

To extract the performances of the chambers (spatial resolution and hit efficiency) an alignment of all wires had to be done first. To this extent we have used several track samples, namely: a) cosmic-ray events stored in between PS spills, as well as beam via a special trigger, b) beam particles, c) tracks emanating from p-target collisions and d) elastic events. The alignment procedure is very involved, since one has to align each one of the NDC modules relative to the others, as well as to the PID detectors (Cherenkov, TOF and electromagnetic calorimeter), the TPC and the Beam detectors. In total more than 15000 parameters have to be adjusted iteratively. After all corrections and iterations, the resulting residual distribution is shown in Fig. 3 and gives a spatial resolution of about 340 μm . This value is about twice worse than what has been measured in the NOMAD conditions. The gas mixture can be invoked here: the longitudinal dispersion of the drifting electrons and the much reduced size of the plateau in the drift velocity distribution as a function of the electric field, both contribute to degrading the resolution. However, one should stress that this spatial resolution is more than sufficient for HARP physics.

3.1.2 Hit efficiency

Hit efficiency can be computed also using several samples of data. Cosmic rays, beam particles (crossing an empty, thin, or thick target) and tracks emanating from an interaction, using the redundancy of NDC modules.

Fig. 4 shows hit efficiencies per measurement plane computed with a large sample of cosmic-ray tracks. The numeration of the modules correspond to the labels in Fig. 1). The average value of the hit efficiency for the central modules lie between 80% and 85%, much lower than the NOMAD conditions (> 95%): this loss of performance can again be attributed to the change of the gas mixture and new electronics. The reduced efficiencies of the two side modules however reflect more a specific degradation with time of chambers which have not been used for about two years (between the NOMAD and HARP data-taking periods).

Fig. 5 shows the hit efficiency for beam particles when a thick target of about one nuclear

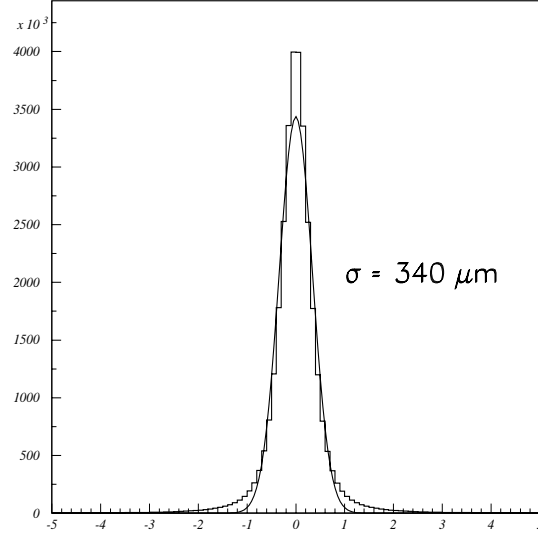


Figure 3: Residuals for a sample of cosmic-ray tracks in the drift chambers.

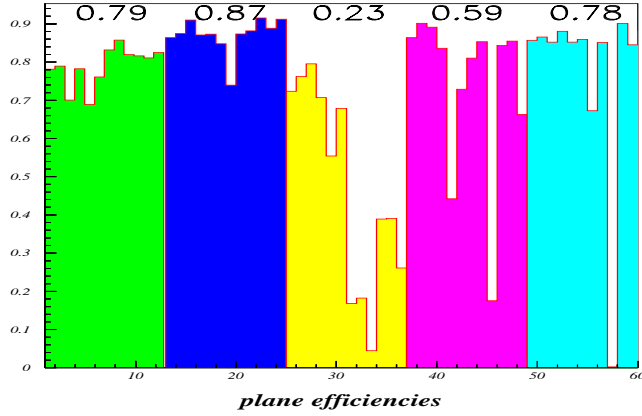


Figure 4: Hit efficiencies of the drift chamber planes, as measured from cosmic-ray data, module by module. Each module is represented with a different color (grey shade). Notice that modules 3 and 4, which have low efficiency are the side modules (see Fig. 1) outside the main fiducial volume.

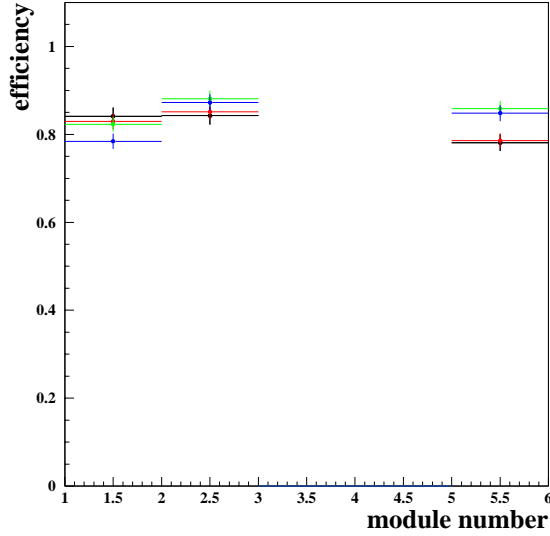


Figure 5: Average hit efficiency per module for 3, 5, 8 and 12 GeV/c thick tantalum data.

interaction length is used. As it can be seen one obtains figures in the vicinity of 80%, consistent with the measurement using cosmic-ray data. Instead, the hit efficiency in module one decreases dramatically if measured with a thin or empty target, as shown in Fig. 6. This is related with chamber saturation due to the high intensity of the beam, as demonstrated by the fact that the efficiency decreases progressively during a spill for no target data (indicating the gradual saturation of the chamber) while remaining constant for thick target data (Fig. 7). The efficiency is close to the nominal value at the beginning of the spill, indicating that the chambers recover between spills.

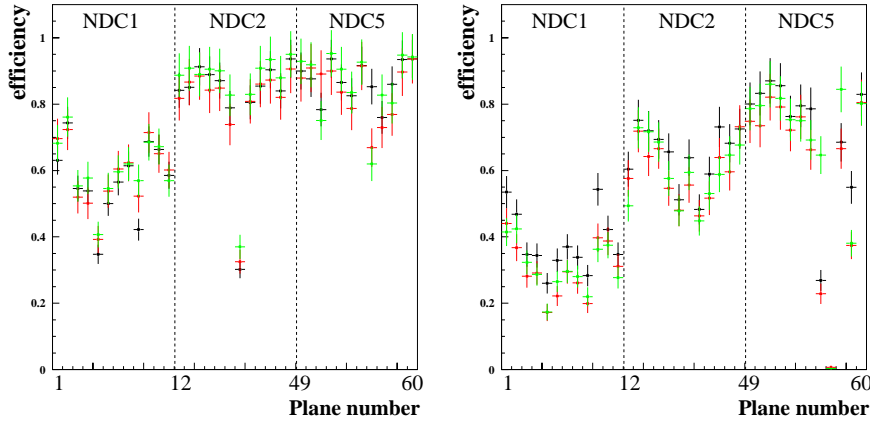


Figure 6: Hit efficiency per plane in modules 1, 2 and 5 for 3 GeV/c (left) and 15 GeV/c (right) empty target data and for 3 different run periods. The efficiency map is similar for thin target.

The hit efficiency can also be computed with interacting particles by reconstructing a track and extrapolating it to a plane (not used in the fit) where a search for a hit is performed around the track extrapolation. In this way one can compute the hit efficiency excluding the beam spot.

Figs. 8 and 9 show respectively the efficiency map for module 1 and modules downstream the spectrometer when the beam spot region is excluded. The data corresponds to different K2K and MiniBooNe settings. Planes with efficiencies below 60% are mostly in module three (Fig. ??), which fortunately is a redundant module.

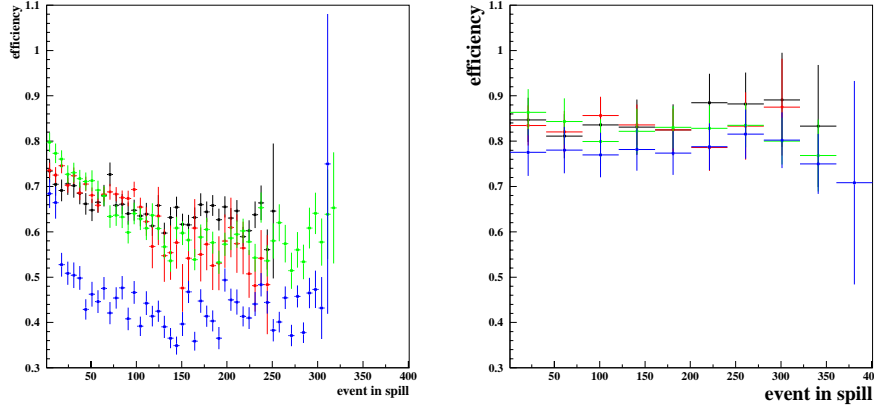


Figure 7: Overall efficiency of module 1 as a function of the event number within a spill for no target (left) and thick tantalum (right) data, and for several beam momenta. The lowest efficiency corresponds to 15 GeV/c. It is important to remark that thin target and no target have similar behaviour.

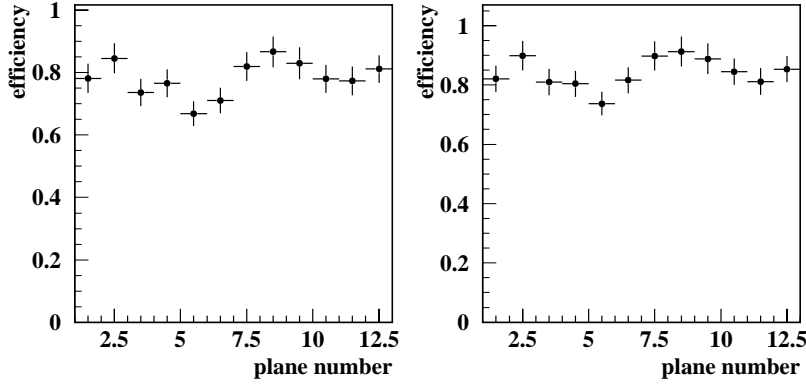


Figure 8: Hit efficiency per plane of module 1 for K2K thick (left) and thin (right) targets. The efficiency is computed with interacting particles outside the beam spot region.

3.2 Cherenkov

The Cherenkov detector consists of a large steel frame with an opening 6 m wide and 3 m high. This frame supports two horizontal rows of 19 photomultipliers each, one row on top and one on the bottom. Fixed to it are also the suspensions of the two sets of mirrors. Two large boxes made of thin walled stainless steel on an aluminium structure define the Cherenkov vessel with a total volume of about 31 m³ filled with perfluorobutane (C_4F_{10}). These boxes are welded directly

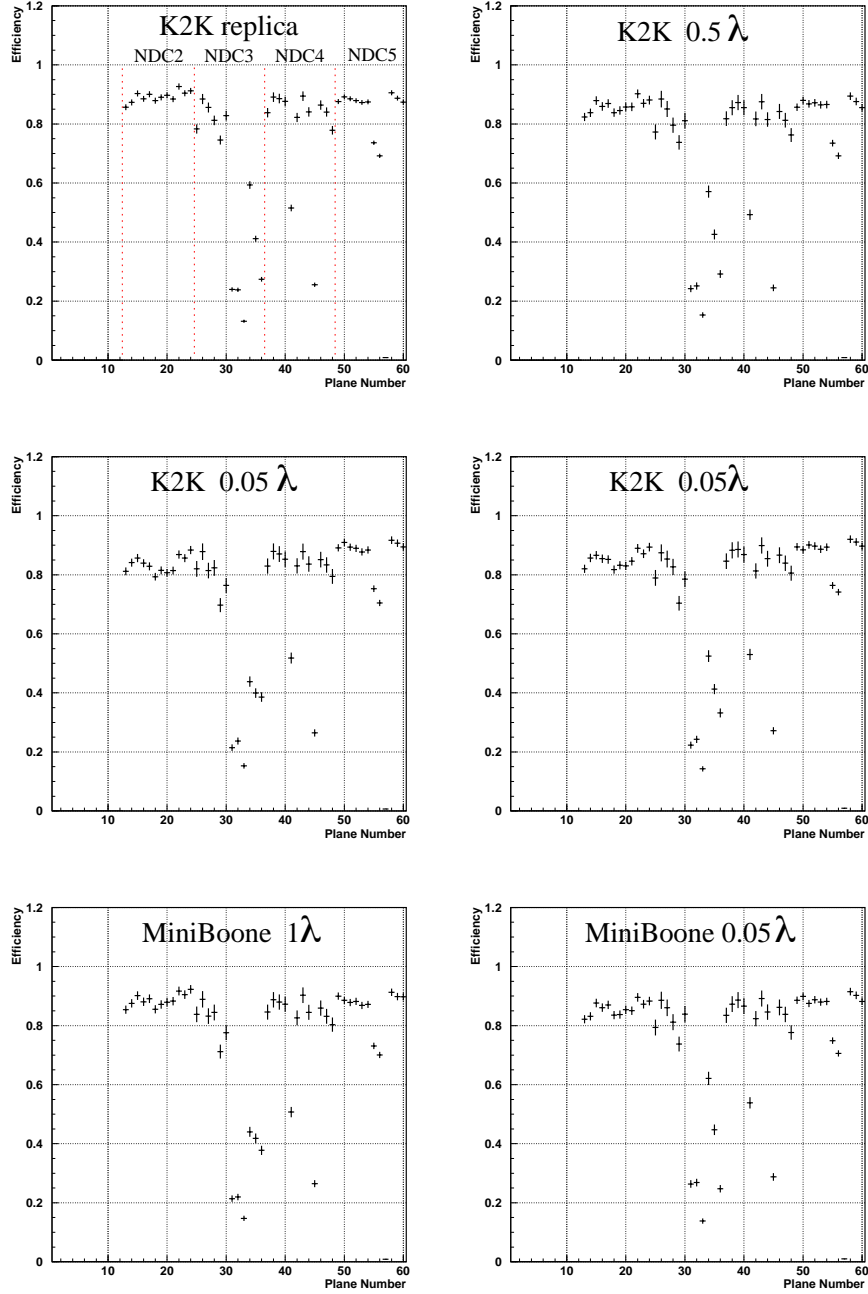


Figure 9: Efficiency per plane in modules downstream the spectrometer for several K2K and MiniBooNe settings. The beam energy is 12.9 GeV/c for K2K and 8.9 GeV/c for MiniBooNe. Plots on the middle have a separation in time of three days.

on the steel frame. They are equipped with large honeycomb panels on the entrance and exit paths of the particles. The total length of the setup along the beam line is 3.5 m. The 8-in diameter EMI 9356-KA photomultipliers were chosen for their very low noise and high gain. In order to increase their useful light collection area to a diameter of 340 mm, the photomultipliers were matched to aluminized Winston cones machined from 150 mm thick PMMA plates.

The particles traverse about 2 m of the radiating medium and generate photons that are deflected by about 135° upwards or downwards by two large cylindrical mirrors 6 m long and with a radius of curvature of 2.4 m. The average reflectivity of the mirrors was about 90%. The light collection system was optimized using the Zemax v.10 optical design software. A light collection efficiency of about 80% was achieved.

A permanent flow of about $6 \text{ m}^3/\text{hour}$ of the gas radiator was continuously maintained by an elaborate gas purification and circulation system.

The device is able to identify electrons below the π saturation momentum ($\sim 4 \text{ GeV}/c$). Pions and electrons can be separated from protons and kaons below the kaon threshold momentum $\sim 9 \text{ GeV}/c$, and protons can be discriminated above this energy. Fig. 10 shows the photoelectron yield for beam pions, electrons and protons, obtained with beam particles of 3 and 5 GeV/c and empty target. Notice that π/e separation is still possible at 3 GeV/c , while π/p separation is quite pure but with a low efficiency. At 5 GeV/c , pions are close to the saturation regime and cannot be distinguished from electrons. Conversely, π/p separation is highly pure and efficient.

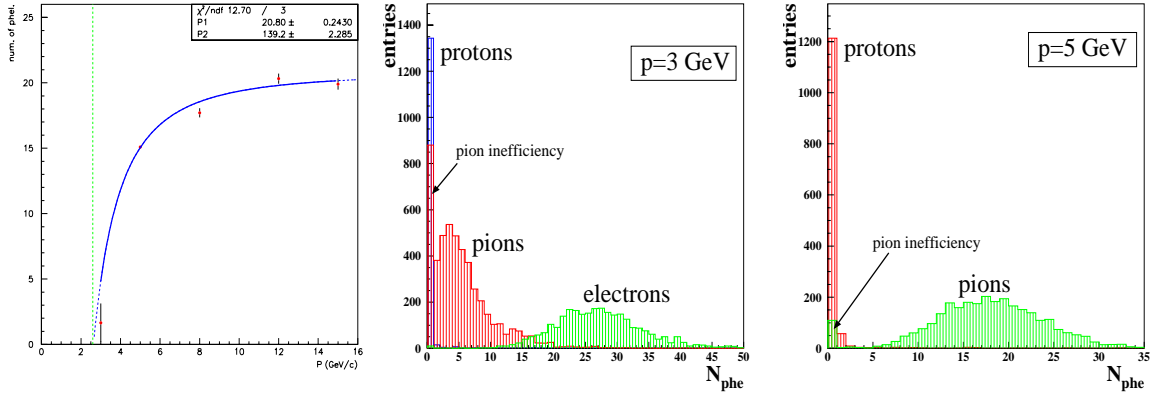


Figure 10: On the left, photoelectron yield as a function of momentum for a selected sample of pions. The experimental points are fitted to the theoretical curve $N_{phe} = N_0 \cdot [1 - (1 + (m/p)^2)/n^2]$, where n is the refraction index of the gas, m is the pion mass, p the momentum and N_0 the photoelectron yield in the saturation regime. The pion threshold is found to be at 2.6 GeV/c . Center and right, photoelectron yield for pions, electrons and protons at 3 and 5 GeV/c respectively. Pure samples are selected using the beam detectors.

3.3 The TOF Wall

The TOF wall detector consists of 39 scintillation counters arranged in three vertical walls placed at about 10 meters from the target and covering an overall area of $657 \times 243 \text{ cm}^2$. In the left/right walls, scintillators are 250 cm long and are oriented vertically, while in the central wall scintillators are 180 cm long and oriented horizontally (see Fig. 11).

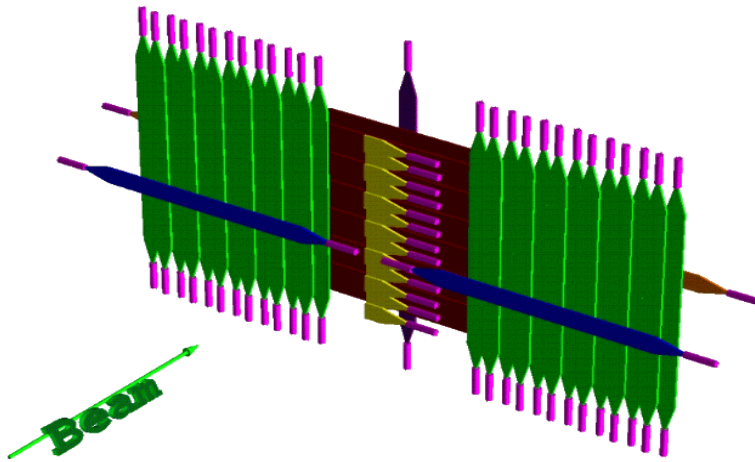


Figure 11: Layout of the TOF Wall detector. The upstream and downstream calibration counters are also shown.

The timing calibration and resolution of the counters were measured in HARP with cosmic muons crossing the TOF wall (For a detailed description of the performance and the calibration procedures see [13]). After these the intrinsic TOF wall resolution is of the order of 150 ps , while the t_0 resolution is close to 70 ps , leading to a combined TOF resolution of about 160 ps , much better than the design value of 300 ps .

Particle identification in the TOF wall relies on the combination of particle momenta, as measured from the forward spectrometer and the time-of-flight between a start signal (t_{start}) from reference counters before the target (TOFB, TOFA and TDS) and a stop signal from the TOF wall itself. The mass of a particle can be computed from these quantities:

$$m^2 = p^2 \cdot [((t_w - t_0) \cdot c/L)^2 - 1],$$

The TOF is able to provide a π/p separation of $\sim 5\sigma$ at $3\text{ GeV}/c$, as can be seen in Fig. 12. This figure also shows the TOF performance for secondary particles in a thin Al target run. In practice, the TOF system will provide reasonable π/p separation up to $4.5\text{ GeV}/c$. The π/k capabilities of the detector at low energies ($< 3\text{ GeV}/c$) are being studied at the moment.

3.4 Electron identifier

The electron identifier is made of two calorimeter planes ($EID1$ and $EID2$) reused from the CHORUS experiment and described elsewhere [14]. It was designed to provide electron-pion separation when low energy ($< 3\text{ GeV}/c$) charged pions, accompanied by knock-on electrons, are occasionally identified as electrons by the cerenkov counter. It also serves to identify electrons at high energy, when the cerenkov has lost its pion/electron separation capabilities.

The detector performance is summarised in Fig. 13 for two different data samples: one including all the particles in an empty target run at $3\text{ GeV}/c$, the other one corresponding to secondary particles in a thin Al target run. The figure shows the yield of particles as a function of $E_1/(E_1 + E_2)$ and $(E_1 + E_2)/p$, where E_1 and E_2 are the energies deposited in $EID1$ and $EID2$ respectively, and p is the momentum. Two well separated populations are clearly visible at $3\text{ GeV}/c$, while in the K2K run a small electron contamination is observed.

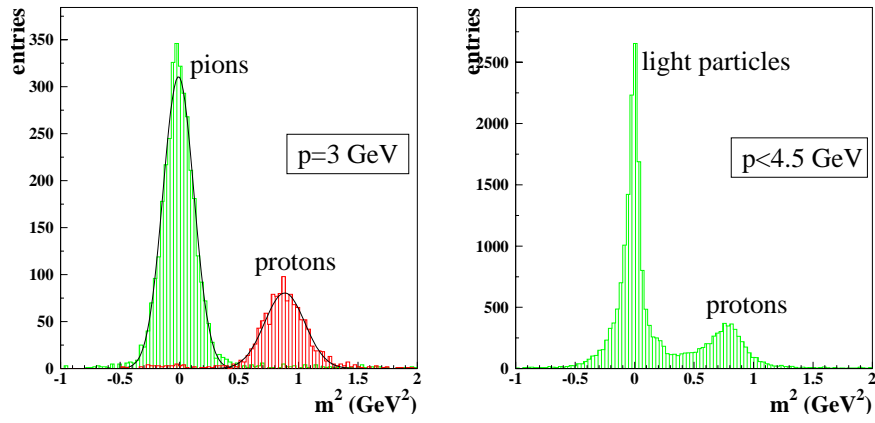


Figure 12: Mass squared as measured by the TOF system for 3 GeV/c no target data (left) and particles below 4.5 GeV/c in a 12.9 GeV/c thin Al target run.

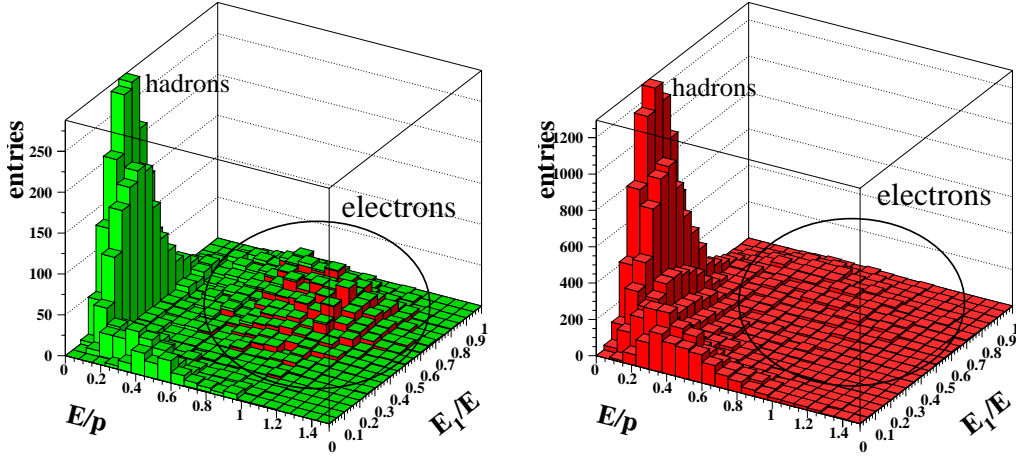


Figure 13: Particle yields as a function of E_1/E and E/p for 3 GeV/c no target (left) and 12.9 GeV/c Al thin target. (right). E is the total energy deposited in the calorimeter ($E_1 + E_2$).

4 Beam Detectors

The beam detectors are of uppermost importance to provide the reference time to the TOF system, and to measure the direction and identity of the incoming particle.

Tracking of incoming beam particles is provided by 4 Multi-Wire Proportional Chambers (MW-PCs). Each chamber has 2 orthogonal wire planes separated by a distance of 10 mm. There are 3 small chambers with a sensitive area of $96 \times 96 \text{ mm}^2$ and 1 mm wire spacing whose wire planes measure the x and y projections, and a fourth with a sensitive area of $196 \times 196 \text{ mm}^2$ and 4 mm wire spacing which is rotated by 45° with respect to the other 3 chambers. Beam particle identification is provided by 2 beam Cherenkovs and a Time Of Flight (TOF) system. Beam Cherenkov A (BCA) is 6 m long and Beam Cherenkov B (BCB) is 3 m long. Both are filled with nitrogen at a pressure which depends on the beam conditions. The TOF system measures flight time over a distance of 21.4 m using 2 scintillator walls made up of 8 scintillator strips.

Figure 14 shows the positions of reconstructed beam particles at the target defining scintillator whose nominal position is indicated by the blue circle. The outline of the scintillator is clearly visible.

The TOF system is utilised for particle identification at low energies separating pions, kaons and protons at 3 GeV/c and 5 GeV/c. A TDC calibration to correct for differences in bin width over the 32 TDC units has been completed. Calibration of ADCs has also been carried out. TOF times corrected using these two sets of calibration constants give a resolution of $\approx 170\text{ps}$ giving excellent particle separation. This can be seen in Figure 15 which shows corrected Time of Flight values for a 3 GeV/c beam.

The Beam Cherenkov are used to tag electrons at low energies where all other particle ID is carried out by the TOF system, and to tag pions at higher energies. Both electron tagging and pion tagging are found to have close to 100 % efficiency. At momenta $> 12\text{GeV}/c$ it is

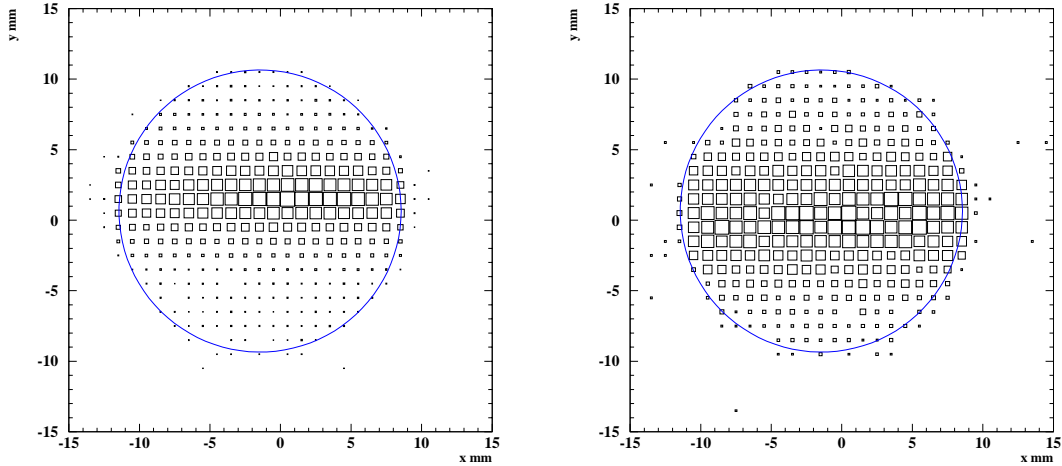


Figure 14: Reconstructed position of beam particles at the target defining scintillator under normal running conditions (left) and for a special alignment run with wide beam (right).

also possible to tag kaons as can be seen in Figure 16 which shows the ADC values from BCA for a 12.9 GeV/c beam. The kaon peak can be clearly distinguished. This technique will be particularly useful for the analysis of data taken with the K2K replica target where a high purity proton beam is required.

5 Forward Tracking

Reconstruction of tracks and momentum measurement in HARP's forward region is made difficult by the meager amount of measurement planes and the rather low efficiency of the chambers ($\sim 80\%$), which prevents a simple approach, such as the one used by the NOMAD experiment, where space points (constructed from a set of three consecutive planes at tilted angles, -5° , 0° , and 5° respectively) were as the basic building block of the track reconstruction algorithm. Such an algorithm is not viable in HARP, since the efficiency to build a space-point (also called triplet) is of the order of $80^3 \sim 50\%$.

Instead, the tracking algorithm in HARP builds three dimensional track segments in each tracking module, with an efficiency larger than 90%. Then, the isolated track segments, together with unused plane segments and hits are combined in order to increase the overall efficiency and the momentum resolution.

In this section we describe our tracking algorithms and discuss two basic ingredients of the cross section calculation, that is the geometrical acceptance and the tracking efficiency.

5.1 The segment algorithm

We have developed a segment algorithm which builds 2D plane segments per module and then combines them to create 3D track segments (also per module). The requirements are the following:

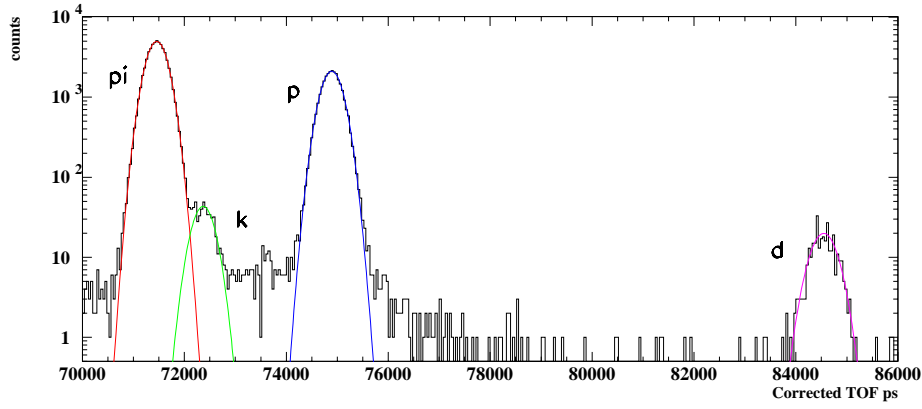


Figure 15: Corrected time of flight values for 3 GeV/c beam (electrons have been removed using information from beam cherenkovs)

- **Plane segment:** At least 3 hits in the same projection (u, x or v) compatible with being aligned. The drift sign associated to each hit is decided during the plane segment reconstruction phase.
- **Track segment:** Two or three plane segments of different projections, whose intersection defines a 3D straight line. In the case of two PS it is also required a hit in the remaining projection compatible with being intersected by the 3D straight line defined by the other two projections.

The above shows that to form a track segment at least seven hits are needed (one per plane) within the same module. The efficiency achieved by this algorithm is of the order of 90%, as shown in Fig. 17. This figure also shows a good agreement between reconstructed data and Monte Carlo simulation.

5.2 The track reconstruction algorithm

The segment algorithm builds isolated plane segments and track segments per module. These can be combined with unused hits to obtain longer track segments and to recover unbuilt track segments. All possible combinations (which include at least a 3D segment) to connect tracking objects in the modules downstream of the dipole magnet are considered. Combinations such as 3D + 2D or even 3D + hits-not-associated are valid ways to build longer, 3D segments.

Matching algorithms are first applied to modules downstream the spectrometer for which the momentum knowledge is not needed (only to estimate multiple scattering). Good matches are merged and refitted. As a example Fig. 18 shows the (track segment)-(track segment) matching residuals between modules 2 and 5.

Notice, however, that to measure the momentum it is in principle sufficient to connect a (3D) segment downstream of the dipole with one space point upstream of the dipole. Since one can impose the constraint that all tracks emanate from the event vertex¹ such point is always known

¹for the thin target analyzed in this paper the vertex is known with a precision of about 1 cm. In the case of thick target, a vertex algorithm will provide the event vertex to a comparable precision.

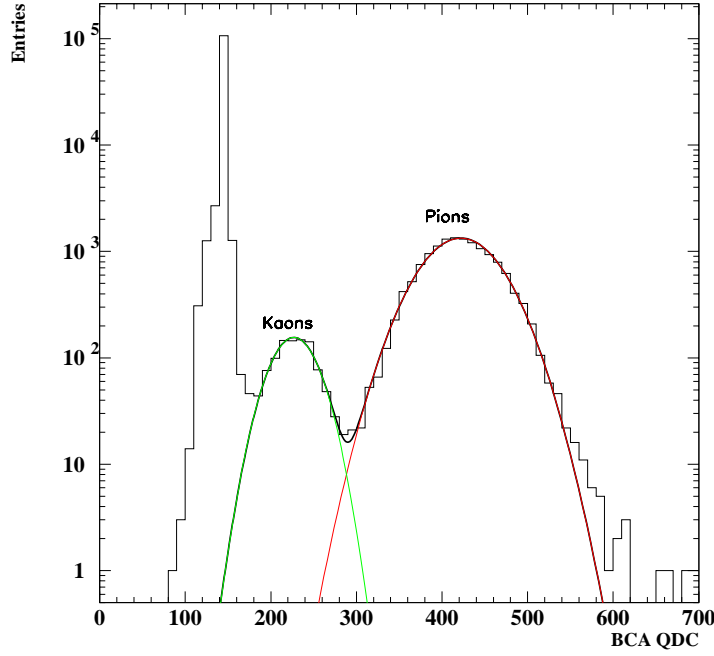


Figure 16: ADC values from Beam Cherenkov A at 12.9 GeV/c

and therefore the necessary and sufficient condition for a particle emanating from the target to have its momentum measured is that a $3D$ segment can be measured by the combination of downstream NDC chambers.

Thus, a measurement in the first NDC module is not strictly necessary to analyse the track momentum. Ideally, one would like, of course, to connect a $3D$ segment downstream with a $3D$ segment in the NDC1 *and* the vertex point. However, the tracking efficiency of the upstream module is sizeable lower than the efficiency of the downstream modules. This is due to, a) a higher hit density in NDC1² and b) the lack of redundance due to the fact that there is only a single module upstream of the dipole. A too restrictive condition to accept a track such as matching a $3D$ segment upstream of the dipole with a $3D$ segment downstream results not only in lower efficiency, but also in a systematic error, arising from the uncertainties in the hit density expected in NDC1 which would be hard to estimate (hit density depends on factors such as track multiplicity and opening angle, which are model-dependent). Instead, by building a track *always* when a $3D$ segment is present downstream of the dipole, one is practically independent of the tracking efficiency in NDC1.

In order to quantify these considerations, we have considered three different types of tracks, depending on the matching between the downstream and upstream modules. Type I is a $3D$ - $3D$ matching. Type II matches a $3D$ (downstream) with a $2D$ (upstream). Type III are those where one has been unable to find either a $3D$ or a $2D$ segment in NDC1 and thus the track is built using the downstream modules and the vertex constraint.

²the hit density decreases quadratically with the distance to the vertex, and therefore the effect is only significant for NDC1.

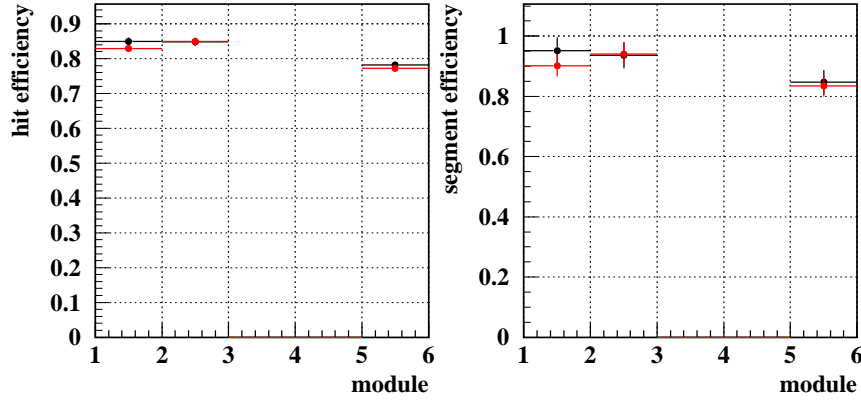


Figure 17: Hit and track segment reconstruction efficiency for 3 GeV/c no target real and Monte Carlo simulated data. The hit efficiency per plane of the data has been introduced in the Monte Carlo simulation.

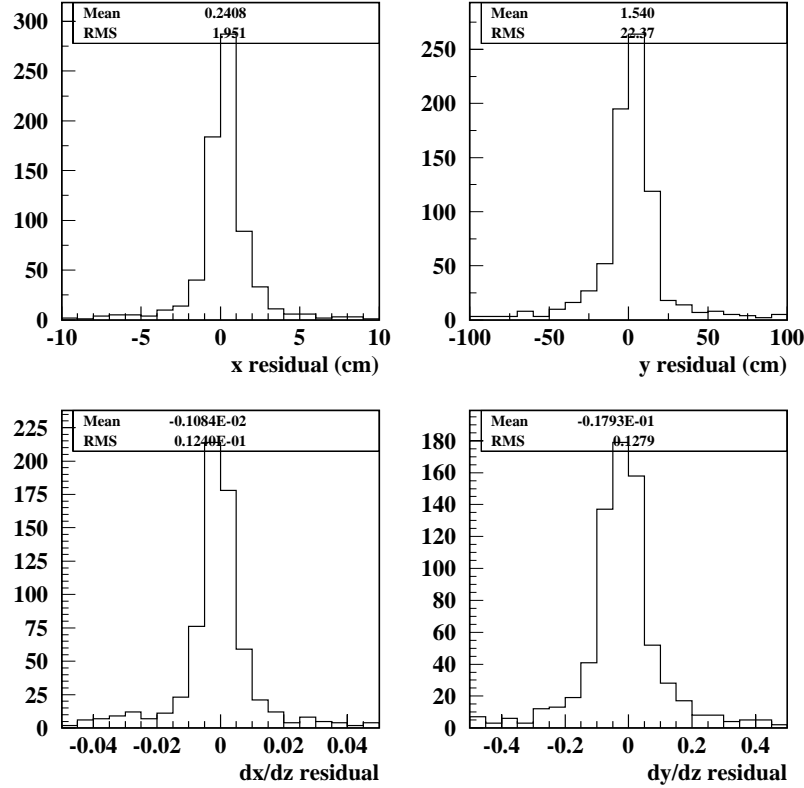


Figure 18: Residuals for the matching between track segments in modules 2 and 5 corresponding to 3 GeV/c no target data.

5.3 Momentum measurement

The matching through the spectrometer requires momentum knowledge, which is estimated during the matching phase. This is done in two steps. In the first step two track segments at either side of the magnet (for type I tracks) are associated to each other by comparison in both the XZ (bending plane) and the YZ plane. A first matching χ^2 is defined through the quantity $\Delta R = R_1 - R_2$ (Fig. 19), assuming a homogeneous magnetic field: $\chi_R^2 = (\Delta R^2 / \sigma_{\Delta R})^2$. A second matching χ^2 is build using the y coordinate and its corresponding slope y' given the fact that the bending in the YZ projection is small. Assuming an average momentum, track segments in NDC1 and NDC2 are extrapolated to the same NDC1 surface to compute the quantity $\chi_y^2 = (\Delta y \ \Delta y')(C_{\Delta y} + C_{\Delta y'})^{-1}(\Delta y \ \Delta y')^T$. The magnetic field inhomogeneities and the non zero bending in the YZ plane will introduce non negligible contributions to χ_R^2 and χ_y^2 respectively, which must be taken into account when applying cuts. In the case of a good matching, a first estimation of the momentum is done taken the weighted average of R_1 and R_2 as the radius of curvature R in the bending plane:

$$p_0 = \frac{0.3 \cdot |R| \cdot B_{avg}}{\sin \alpha} \quad (1)$$

where α is the angle between the initial momentum and the magnetic field, and B_{avg} is the average magnetic field, which turns out to be 0.325 Tesla. The initial charge will be $q_0 = R/|R|$.

The second step consists in looping over momenta around p_0 to obtain a χ^2/ndf versus p distribution, which is fitted to a parabola. The momentum and its error are then computed using the equation of the parabola.

The momentum resolution (as a function of the momentum) achieved with this method is shown in Fig. 20. Notice the excellent agreement between data and MC.

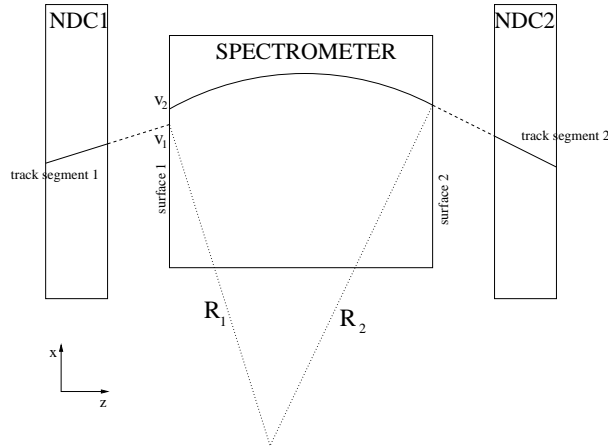


Figure 19: Matching through the spectrometer. v_1 is the state vector of track segment 1 extrapolated to the spectrometer entrance and v_2 the state vector of track segment 2 extrapolated to the spectrometer exit. The intersection of the normal to the track extrapolations in the bending plane defines the two radius R_1 and R_2 . These should be comparable for track segments belonging to the same particle.

For track types II and III the procedure is identical except that one matches a 3D segment downstream de magnet with the vertex point (and with a2D segment for track type II). Figures

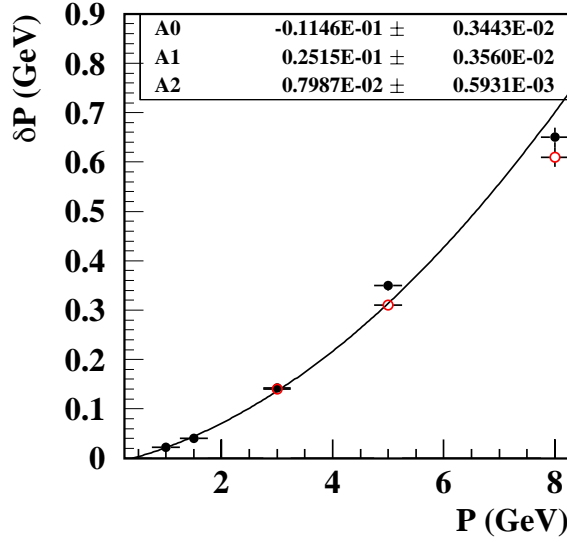


Figure 20: Momentum resolution for 1, 1.5, 3, 5 and 8 GeV/c empty target Monte Carlo data, and for 3, 5 and 8 GeV empty target data. The curve represents the fit of the MC points to a parabola. The agreement between data and MC is excellent.

21 and 22 show the momentum resolution as a function of momentum for these track types.

Figure 21: Momentum resolution for 1, 1.5, 3, 5 and 8 GeV/c empty target Monte Carlo data, and for 3, 5 and 8 GeV empty target data for track type II. The curve represents the fit of the MC points to a parabola. The agreement between data and MC is excellent.

Figure 22: Momentum resolution for 1, 1.5, 3, 5 and 8 GeV/c empty target Monte Carlo data, and for 3, 5 and 8 GeV empty target data for track type III. The curve represents the fit of the MC points to a parabola. The agreement between data and MC is excellent.

5.4 Geometrical acceptance

The geometrical acceptance $\varepsilon_{i\alpha}^{acc}$ of the spectrometer is defined as the ratio between the true particle yield $N_{i\alpha}$ and the yield accepted by the dipole $N_{i\alpha}^{acc}$, where the index i runs over bins of true momentum and production angle, and the index α refers to the particle type (pion, electron, etc). This index is necessary because the acceptance is, a priori, different for different particle types (consider for example electron bremsstrahlung).³ The geometrical acceptance can be computed with the Monte Carlo, provided that the description of the apparatus geometry

³SO WE NEED TO COMPARE THE ACCEPTANCE OF SAY, ELECTRONS AND PIONS TO FIND OUT HOW DIFFERENT IF AT ALL THEY ARE

and the dipole magnetic field map are accurate⁴.

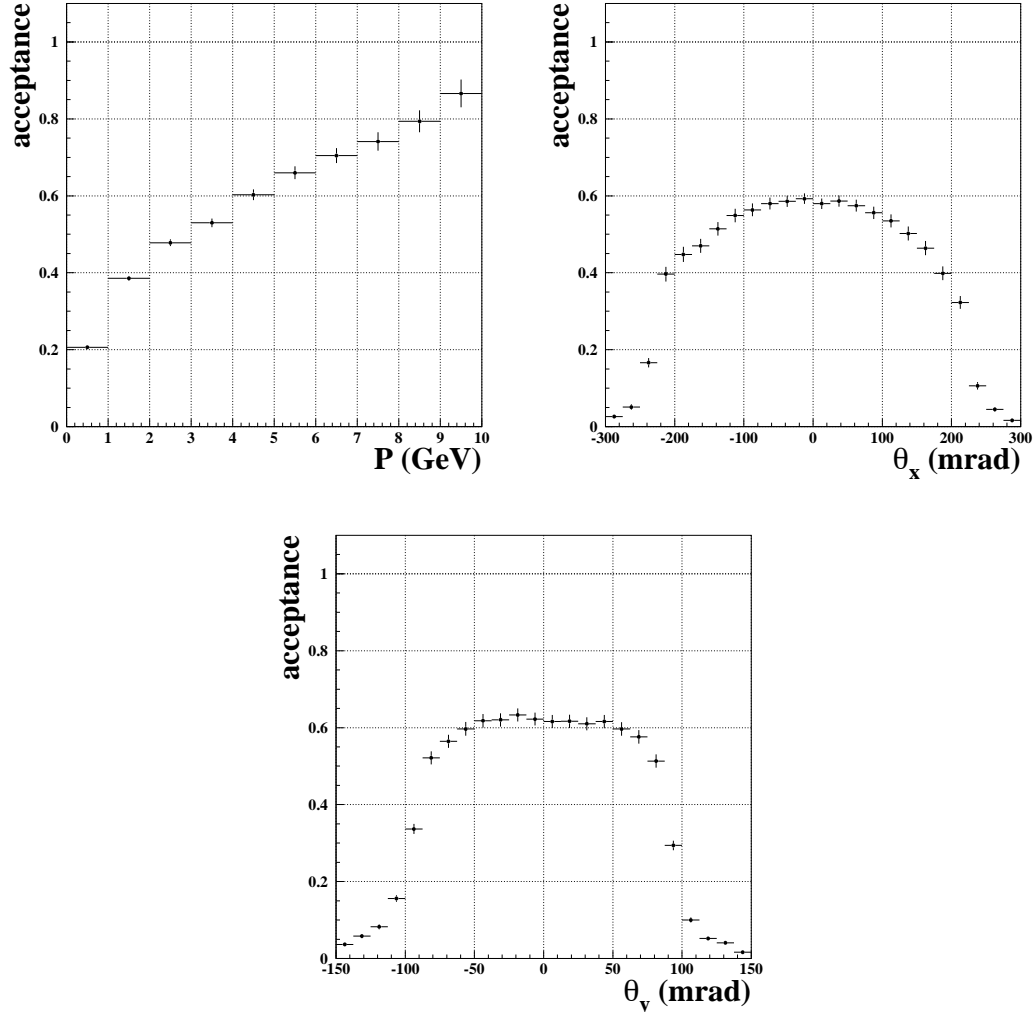


Figure 23: Acceptance for no cuts.

Fig. 35 shows the (pion) acceptance in bins of momentum (left) θ_x (center) and θ_y (right), where θ_x and θ_y are the cartesian components of the production angle θ . Given the dipole dimensions, the acceptance in θ_y is rather small, about 50 mrad. However, given the azimuthal symmetry of the cross-section this is not a problem. Fig. 24 shows the acceptance in bins of momentum (left) and θ_x (right) when a cut on $|\theta_y| < 50 \text{ mrad}$ is imposed. Since momentum and angle are correlated, Fig. 25 shows the acceptance in bins of momentum (left) when cuts on $|\theta_y| < 50 \text{ mrad}$, $|\theta_x| < 200 \text{ mrad}$ are imposed and the acceptance in bins of θ_x (right) when cuts on $|\theta_y| < 50 \text{ mrad}$ and $P > 1 \text{ GeV}$ are imposed.

Notice that both the momentum and angle acceptance are well matched to the requirements of K2K (see section 2).

⁴SO WE NEED TO DEMONSTRATE THAT MAGNETIC FIELD MAP IS OK ALSO FOR ACCEPTANCE CALCULATION!!

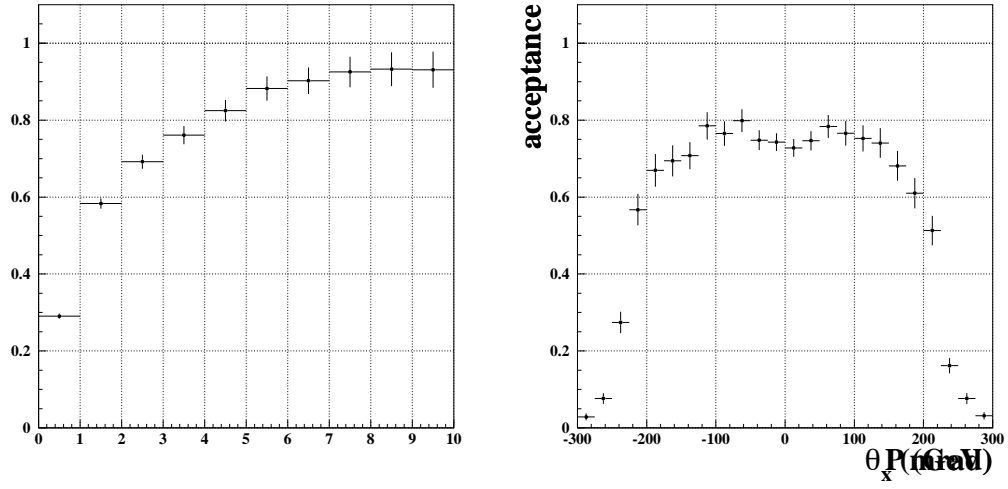


Figure 24: Acceptance for $|\theta_y| < 50\text{mrad}$

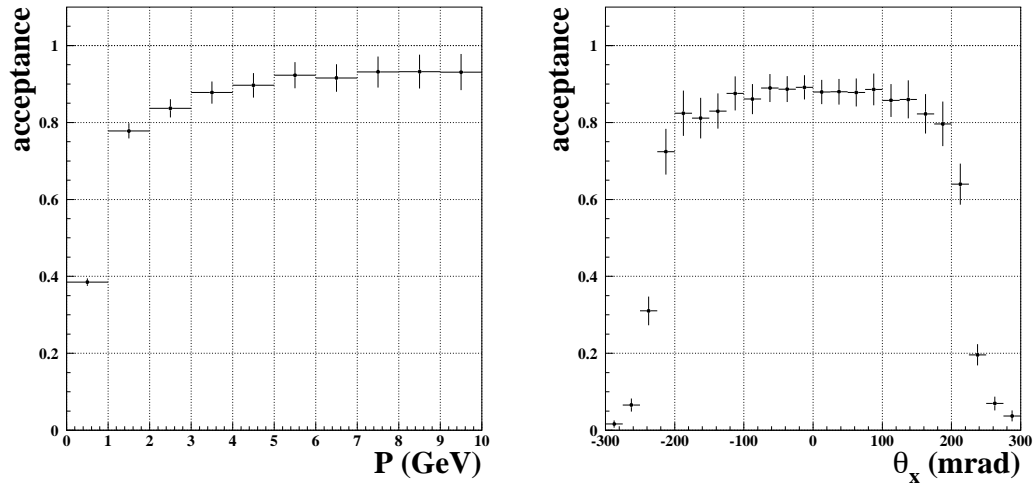


Figure 25: Acceptance in P for $|\theta_y| < 50\text{mrad}$, $|\theta_x| < 200\text{mrad}$. Acceptance in θ_x for $|\theta_y| < 50\text{mrad}$ and $P > 1\text{GeV}$

5.5 Tracking efficiency

Tracking efficiency can be defined as:

$$\varepsilon_i^{track} = \frac{N_i^p}{N_i^{acc}} = \frac{N_i^{down}}{N_i^{acc}} \cdot \frac{N_i^p}{N_i^{down}} = \varepsilon_i^{down} \cdot \varepsilon_i^{up-down} \quad (2)$$

where,

- N_i^{acc} is the number of primary particles accepted,
- N_i^p is the number of primary particles with momentum measured,
- N_i^{down} is number of primary particles accepted with a reconstructed track segment downstream the dipole
- ε_i^{down} is the downstream tracking efficiency,
- $\varepsilon_i^{up-down}$ is the up-down matching efficiency.

The quantity $\varepsilon_i^{up-down}$ can be easily computed with both data and Monte Carlo samples. In both cases, one just needs to count how many times a valid track segment downstream the dipole (that is a 3D track segment) is matched either to another track upstream the dipole or to the vertex point itself. ⁵

Fig. 26, 27 and 28 show $\varepsilon_i^{up-down}$ for data (upper), Monte Carlo (middle) and the reatio between both (lower), for the three track types considered.

Figure 26: $\varepsilon_i^{up-down}$ for data (upper), Monte Carlo (middle) and the reatio between both (lower), for track type I

Figure 27: $\varepsilon_i^{up-down}$ for data (upper), Monte Carlo (middle) and the reatio between both (lower), for track type II

Figure 28: $\varepsilon_i^{up-down}$ for data (upper), Monte Carlo (middle) and the reatio between both (lower), for track type III

To compute the downstream tracking efficiency one can use the redundancy offered by the modules downstream the target. Since there are always at least two overlapping modules one can compute the probability of reconstructing a track downstream using elementary probability.

⁵SO WHAT? DO WE USE DATA OR MC? DO WE TUNE OR DO WE COMPUTE A CORRECTION FACTOR

The probability of reconstructing a track in module “A” given a track reconstructed in module “B” is:

$$P(A \cup B) = P(A) + P(B) - P(A \cap B) \quad (3)$$

$$P(A \cap B) = P(A) \cdot P(B|A) \quad (4)$$

since the probability of reconstructing a track in a given module is independent of the probability of reconstructing it in a different module, $P(A \cap B) = P(A) \cdot P(B|A) = P(A) \cdot P(B)$.

Thus, if we consider, for example, only modules 2 and 5:

$$\varepsilon_i^{down} = \varepsilon_i^{NDC2} + \varepsilon_i^{NDC5} - \varepsilon_i^{NDC2} \cdot \varepsilon_i^{NDC5} \quad (5)$$

Considering all the downstream modules:

$$\begin{aligned} \varepsilon_i^{down} &= \sum_m \varepsilon_i^m - \sum_{m_1 \neq m_2} \varepsilon_i^{m_1} \cdot \varepsilon_i^{m_2} + \sum_{m_1 \neq m_2 \neq m_3} \varepsilon_i^{m_1} \cdot \varepsilon_i^{m_2} \cdot \varepsilon_i^{m_3} = \\ &= \varepsilon_i^2 + \varepsilon_i^3 + \varepsilon_i^4 + \varepsilon_i^5 \\ &\quad - \varepsilon_i^2 \cdot \varepsilon_i^5 \\ &\quad - \varepsilon_i^2 \cdot \varepsilon_i^3 \\ &\quad - \varepsilon_i^2 \cdot \varepsilon_i^4 \\ &\quad - \varepsilon_i^3 \cdot \varepsilon_i^5 \\ &\quad - \varepsilon_i^4 \cdot \varepsilon_i^5 \\ &\quad + \varepsilon_i^2 \cdot \varepsilon_i^3 \cdot \varepsilon_i^5 \\ &\quad + \varepsilon_i^2 \cdot \varepsilon_i^4 \cdot \varepsilon_i^5 \end{aligned} \quad (6)$$

where ε_i^m is the m -module efficiency for the bin i , including the module acceptance. If we separate now tracking efficiency and acceptance

$$\varepsilon_i^m = \varepsilon_i^{acc-m} \cdot \varepsilon_i^{track-m} \quad (7)$$

It is possible to compute the module tracking efficiency both from Monte Carlo and the data themselves using the following procedure, sketched in Fig. 29.

- select a given module, “M”.
- count all downstream tracks with a minimum amount of hits inside a road in M (e.g, five hits). This quantity goes to the denominator.
- count the downstream track which match a reconstructed track segment in M. This quantity goes to the numerator.

That is

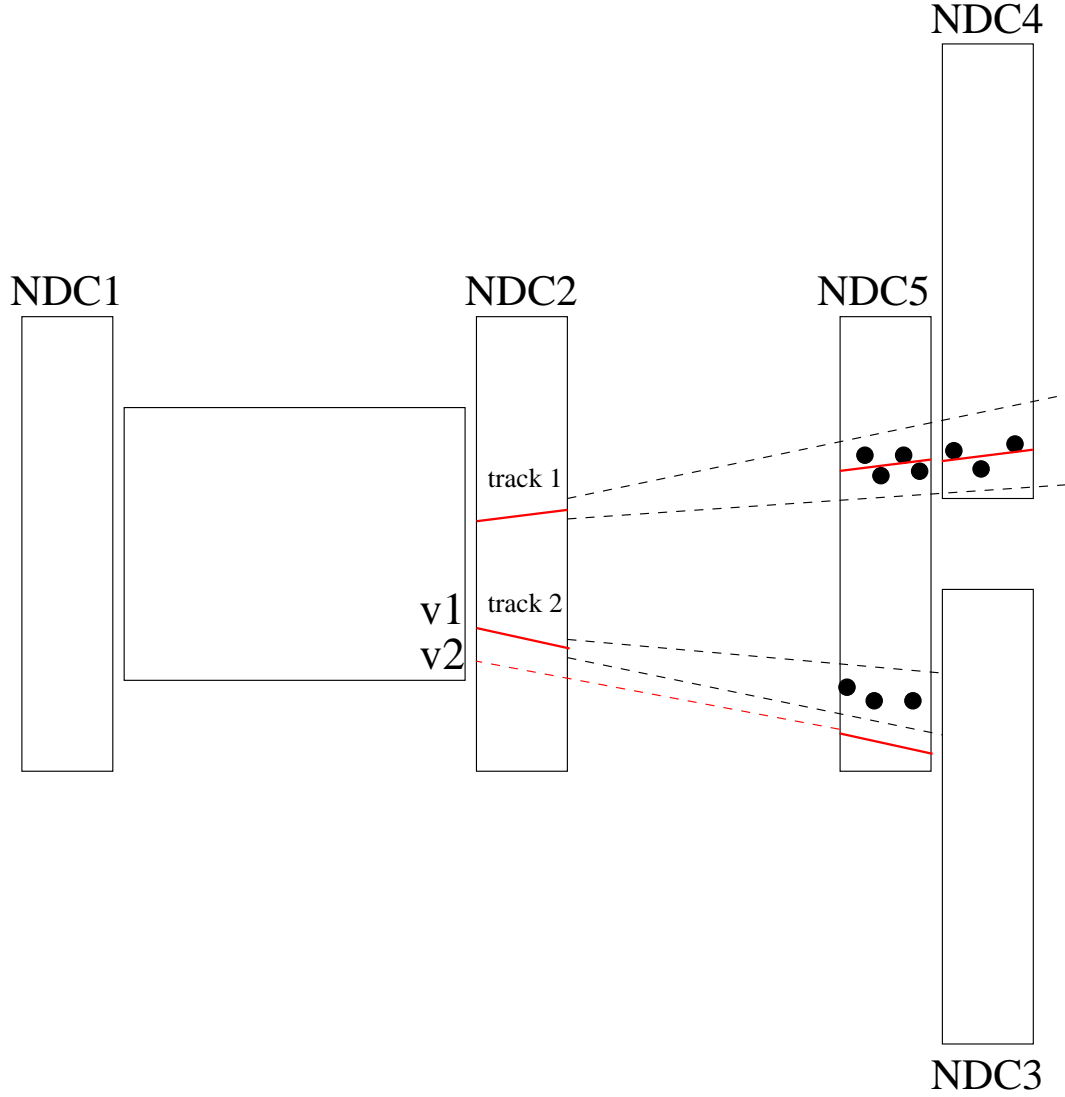


Figure 29: Method for computing the module efficiency. Track 1 is extrapolated to modules 5 and 4. If there are more that 5 hits in module 5 inside the road, we put it in the denominator. If we find a track inside the road we put it also in the numerator. To handle the case of unsuficiely wide roads, the botton case is also used. If the track in module 5 is not inside the road of track in module 2 we extrapolate both tracks to the first plane of module 2 and compare the extrapolations ($v1$ and $v1$). If they are consistent to each other it will contribute to the numerator.

$$\varepsilon_i^{acc-m} = \frac{N_i^{acc-m}}{N_i^{acc}} = \frac{\text{particles with } N_{hits}^m \geq 5}{\text{particles with } N_{hits}^2 \geq 5} \quad (8)$$

$$\varepsilon_i^{track-m} = \frac{N_i^{t-m}}{N_i^{acc-m}} = \frac{\text{particles with a track segment in module } m}{\text{particles with } N_{hits}^m \geq 5} \quad (9)$$

Figure 30: Downstream module tracking efficiency for data (upper), Monte Carlo (middle) and the reatio between both (lower), for track type I

Fig. 30 show the downstream module tracking efficiency (for type I tracks) computed using Monte Carlo and the data themselves. The disagreement between both quantities is due to the fact that the segment-to-segment matching χ^2 distribution observed in the data is not well reproduced by the Monte Carlo, as illustrated in Fig. 31. This is due to a combination of several effects in the simulation of the drift chamber parameters, in particular the non-linearity of the time-to-distance relation, which leads to a dependency of the resolution with track angle.

Figure 31: Segment-to-segment matching χ^2 for data (upper), Monte Carlo (middle) and the reatio between both (lower), for tracks type I

The module acceptance, on the other hand, is safely computed using the Monte Carlo since it depends only of geometrical description. Fig. 33 and 34 show the module efficiency and acceptance respectively.

In principle, downstream tracks do not have the production momentum and angle measured. In that case how can we know the corresponding bin (in ε_i^{down} or ε_i^{NDC2})? . We must have a relation between the extrapolation to NDC2, which is available for all downstream tracks considered (x_2 , y_2 , θ_{x2} and θ_{y2}), and the production quantities p and θ . Fortunately, the tracking efficiency of the modules downstream the dipole (2,3,4,5) can be assumed independent of x_2 and θ_{x2} . Indeed, variations of 10% in the tracking efficiency of the individual modules correspond to variations of 1% in the overall downstream efficiency, which can be neglected at this level.

The downstream efficiency is nearly flat on p and θ_x , with a value of 98%. The deviation from this value is of the order of 1.5%

The up-down matching efficiency is computed as follows:

$$\varepsilon_i^{up-down} = \frac{N_i^p}{N_i^{down}} = \frac{\text{primary particles with momentum measured}}{\text{primary particles with a downstream track segment}} \quad (10)$$

Although the absolute efficiency is larger in the monte carlo, the agreement between the shapes of the distributions is excellent. A larger absolute efficiency in the MC can be explained as a consequence of saturation. Indeed, the saturation effect is known to be optimistic in the MC, leading to a larger frequency of type 1 tracks, which are in general more efficient.

Being the shapes of data and MC very similar one can scale the MC to reproduce the data and use the first to compute the up-down matching efficiency in terms of the production quantities

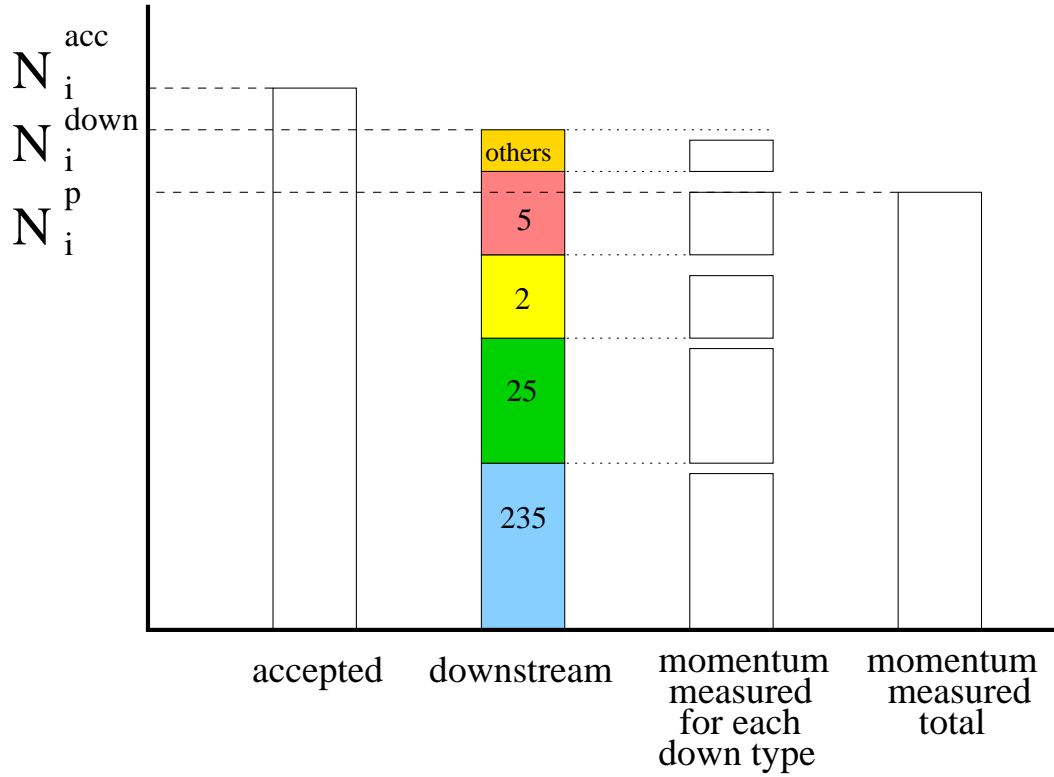


Figure 32:

p and θ . The correction must be done independently for the three track types and then add the individual efficiencies to obtain the total tracking efficiency. The scaling factors are: (0.81, 0.95, 1.34) for monte carlos 1 and 2 respectively (0.91, 0.81, 1.2).

The corrected distributions for MC1 are shown in Fig 37. Fig. 38 shows the comparison between the two hadron generators. The final up-down matching efficiency is shown in Fig. ?? and ??

6 PID

7 Cross Section Calculation

8 Conclusions

Acknowledgements

We wish to thank the IT/DB group of the IT Division at CERN and personally to Andrea Valassi for designing and executing the migration of the Harp data and software from Objectivity to the new storage system based on Oracle. We would also like to thank the IT/ADC and IT/DS groups for contributing to the setup of the migration infrastructure and allocating the relevant hardware resources.

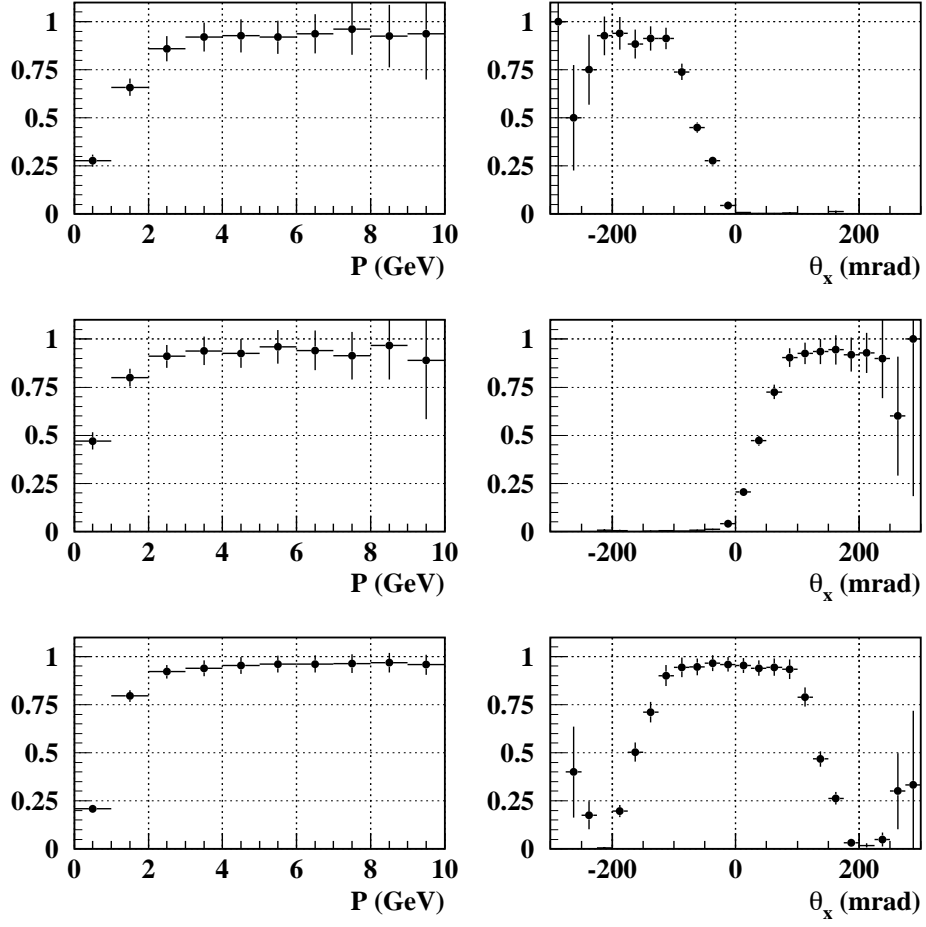


Figure 33: Acceptance of modules 3, 4 and 5 normalized to the acceptance of module 2, as function of p and θ_x

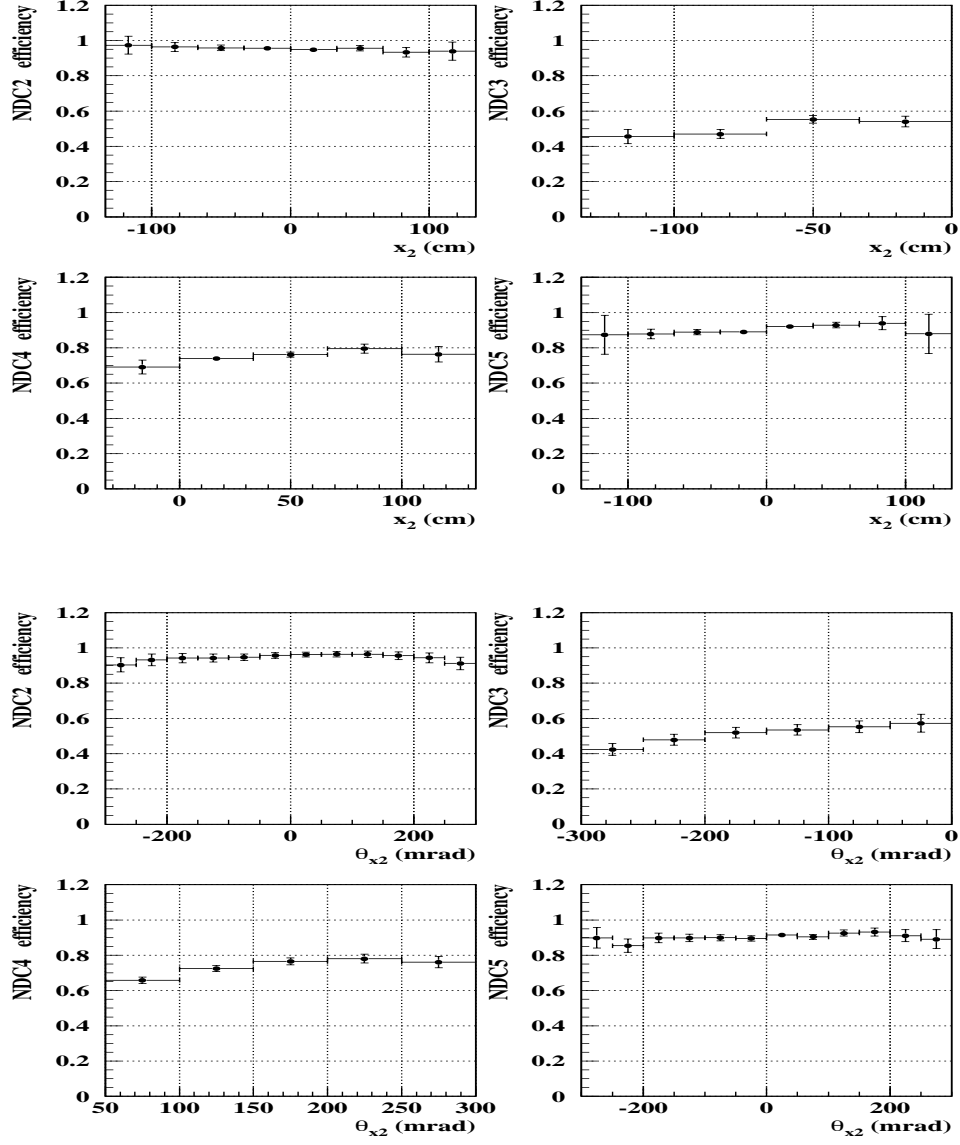


Figure 34: Tracking efficiency of modules downstream the dipole as a function of x_2 and θ_{x2}

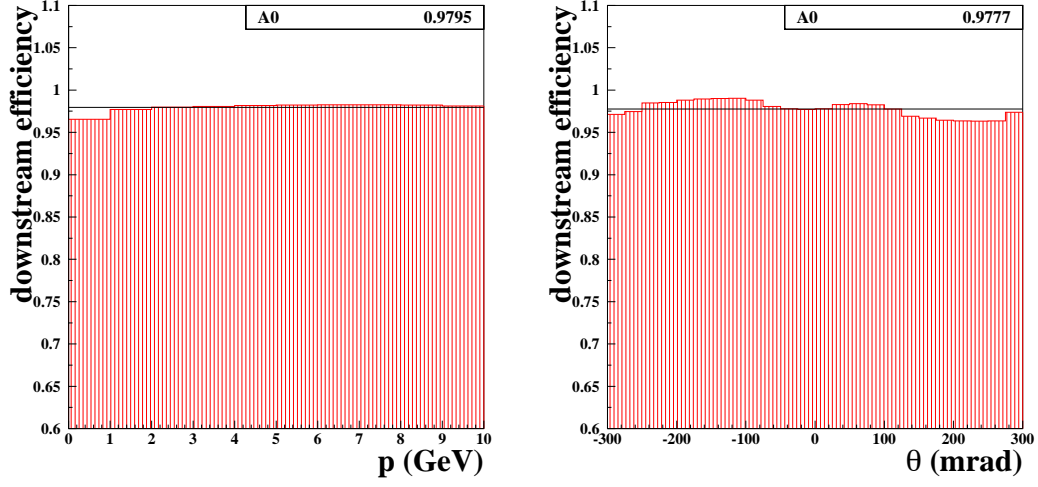


Figure 35: Downstream efficiency as a function of p (left) and θ_x (right).

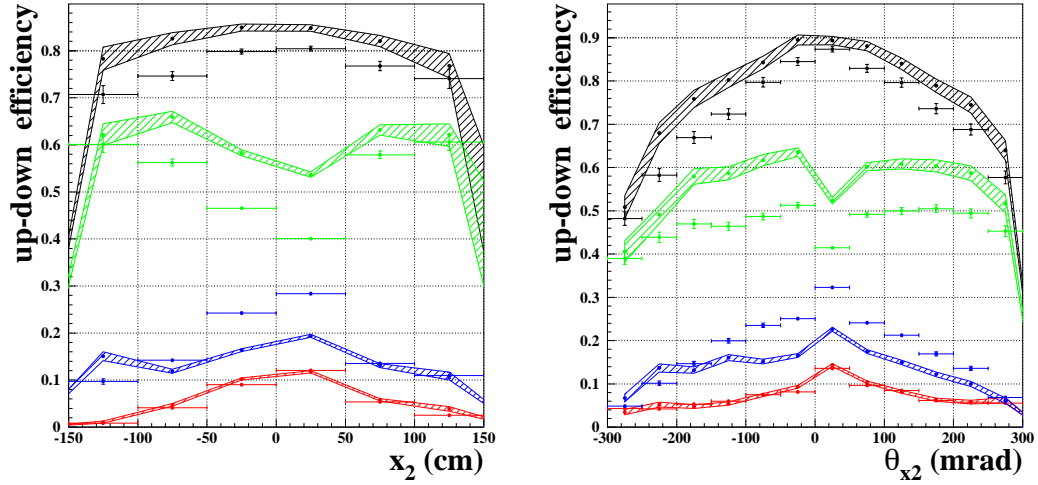


Figure 36: Up-down matching efficiency as a function of x_2 (left) and θ_{x2} (right), for data (points) and MC (boxes).

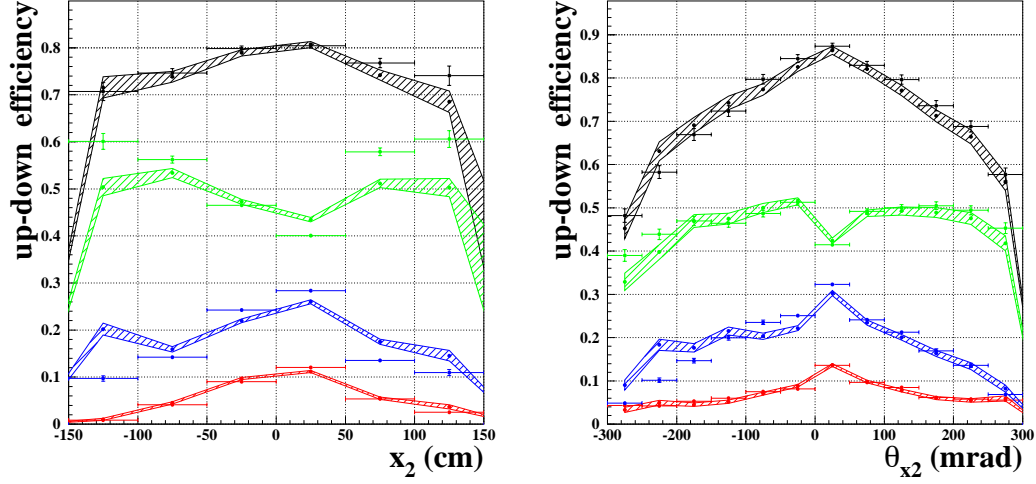


Figure 37: Up-down matching efficiency as a function of x_2 (left) and θ_{x_2} (right), for data (points) and MC (boxes). The MC has being normalized to the data individually for the 3 track types. The total efficiency is the sum of the normalized efficiency for each type.

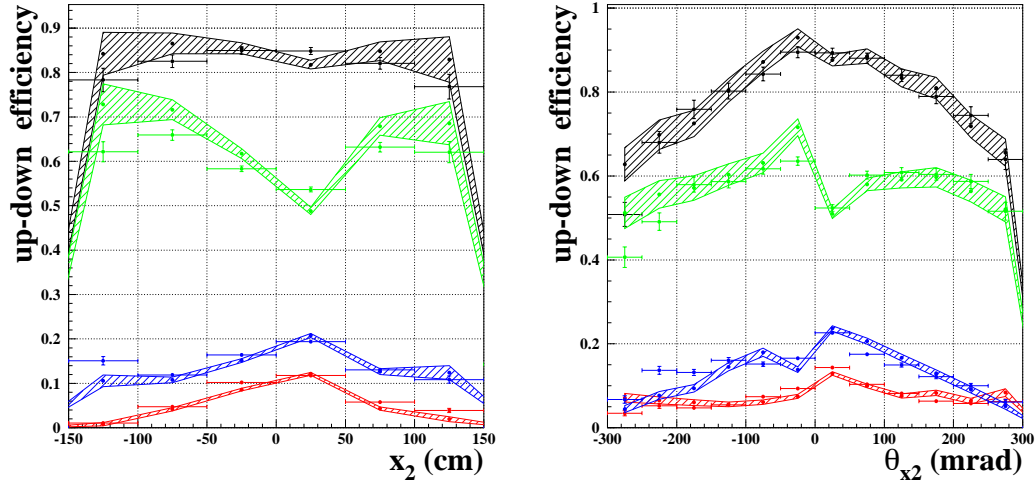


Figure 38: Up-down matching efficiency as a function of x_2 (left) and θ_{x_2} (right), for two different MC generators normalized to each other. s a function of x_2 (left) and θ_{x_2} (right), for data (points) and MC (boxes). The second MC (boxes) has being normalized to the first MC individually for the 3 track types. The total efficiency is the sum of the normalized efficiency for each type.

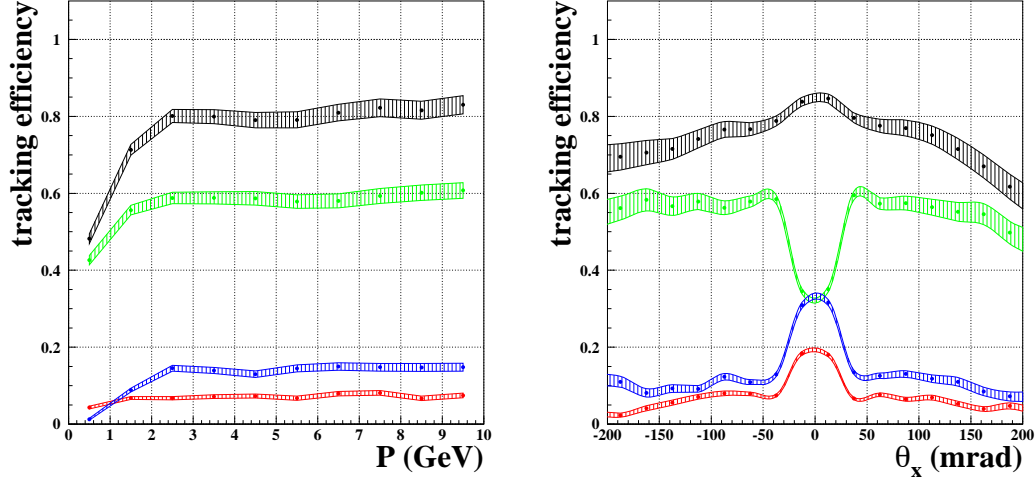


Figure 39: Total tracking efficiency as a function of p (left) and θ_x (right) for MC. The MC has been normalized to the data individually for the 3 track types. The total efficiency is the sum of the normalized efficiency for each type. The colors indicate: black=total, green=type 1, red=type 2, blue= type 3.

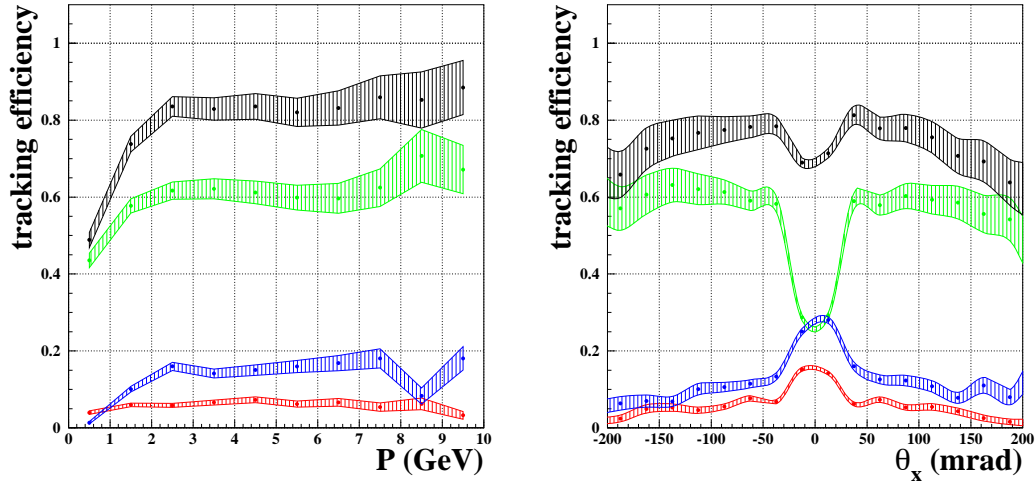


Figure 40: Total tracking efficiency as a function of p (left) and θ_x (right) for MC (second generator). The MC has been normalized to the data individually for the 3 track types. The total efficiency is the sum of the normalized efficiency for each type. The colors indicate: black=total, green=type 1, red=type 2, blue= type 3.

References

- [1] The HARP Collaboration, CERN-SPSC/2003-027, SPSC-P-325
- [2] For a recent review of the neutrino factory see, for example J.J. Gomez-Cadenas and D.A. Harris, Ann.Rev.Nucl.Part.Sci.52:253-302,2002e
- [3] See for example G.D. Barr et al., Phys.Rev.D70:023006,2004.
- [4] I. Stancu *et al.* MiniBooNE collaboration, “*The Miniboone Detector Technical Design Report*”, FERMILAB-TM-2207.
- [5] M. H. Ahn *et al.* K2K Collaboration, “*Indications of neutrino oscillation in a 250-km long-baseline experiment*”, Phys. Rev. Lett. **90** (2003) 041801.
- [6] CERN-SPSC/2000-029.
- [7] CERN-SPSC/2001-031.
- [8] CERN-SPSC/2002-013.
- [9] CERN-SPSC/2002-019.
- [10] CERN-SPSC/2003-27.
- [11] CERN-SPSC/2004-018.
- [12] M. Anfreville *et al.*, Nucl. Instr. and Meth. **A481** (2002) 339.
- [13] M. Baldo-Ceolin et al, Nucl. Instr. and Meth. **AXXX**
- [14] The CHORUS Collaboration, Nucl. Instr. and Meth. A349 (1994) pp.70-80.
The CHORUS Collaboration, Nucl. Instr. and Meth. A378 (1996) pp.221-232.
- [15] D.Panayotov, HARP internal note, in preparation.
- [16] Geant4 Collaboration, Nucl. Instrum. Meth. A **506** (2003) 250.
- [17] G. Vidal, “*The HARP Time Projection Chamber*”. Ph-D Thesis,CERN-THESIS-2003-011.
- [18] A. Lundborg, “*The Time Projection Chamber of the HARP Experiment*”, Diploma thesis, CERN-THESIS-2002-031.
- [19] R. Fruwirth, “*Application of Kalman filtering techniques to track and vertex fitting*” Nucl. Instr. and Meth. A262 (1987) 444.
- [20] G. Prior and A. Cervera, “*Vertex fit using Kalman Filter*”
<http://ps-proj-hadroprod-analysis.web.cern.ch/ps-proj-hadroprod-analysis/AnalysisNotes/notes.htm>
- [21] Nucl.Phys. B (Proc. Suppl.) 125C pp.37-42
- [22] S. Borghi et al., “*Clustering algorithm*”, HARP-note-May 2003.
- [23] J. Utterwijk “*A Chorus Pattern Recognition Algorihm*”, Chorus note in preparation.
- [24] Aleph Collaboration, “*Reconstruction algorithms for Aleph*”, ALEPH-88-4, May 3, 1988.
- [25] N.I. Chernov,G.A.Ososkov - CCC 33(1984) 329-333